Sensorless Control with Fault-Tolerant Ability for Switched Reluctance Motors

Xiaodong Sun, *Senior Member, IEEE*, Xingtao Tang, Xiang Tian, Gang Lei, *Member, IEEE*, Youguang Guo, *Senior Member, IEEE*, and Jianguo Zhu, *Senior Member, IEEE*

***Abstract*—This paper presents a new sensorless control strategy with the fault-tolerant ability for switched reluctance motors (SRMs). Nowadays, many rotor position detection methods are utilized, but most of them increase the system cost due to the additional hardware or complex calculations. To address this problem, various methods of using phase inductance to estimate the rotor position and speed have been proposed. However, the traditional inductance detection method will cause signal distortion due to the presence of interference signals and the unbalanced phase inductance. In particular, the turn-ON angle is advanced. To further improve the stability of the control system, the interference signals are eliminated via establishing the reference time of the inductance characteristic point and the error band in this work. When the position signal disappears, the inductance characteristic points of adjacent phases will be adopted for signal compensation to realize fault-tolerant control. Finally, an SRM drive system is used to verify the effectiveness of the proposed control strategy.**

***Index Terms*—fault-tolerant ability, inductance inflection point, sensorless control, switched reluctance motor.**

I. Introduction

THANKS to the features of simple structure, low price, flexible control, and high operating efficiency switched reluctance motors (SRMs) are widely applied in aerospace, electric vehicles, and precision machining [1]-[3]. To improve the stability and dynamic performance, SRMs require the information of precise rotor position and speed. However, the installation and utilization of mechanical sensors will not only increase the cost and complexity of the drive system, but also increase the potential risk of the control system [4]. Therefore, various position sensorless control methods have been developed to overcome these disadvantages. Meanwhile, various control methods have been proposed to weaken the shortcoming of the double salient pole structure [5].

A. Related research

In the last three decades, many methods have been investigated to improve the performance of SRMs, including structural optimization [6]-[8], direct torque control [9], sensorless control [10]. In particular, sensorless control methods have been proposed increasingly. According to the features of the estimated rotor position, the main control schemes can be classified into three categories, i.e., modern control theory-based methods [11]-[15], flux-linkage-based methods [16]-[19], and inductance characteristics-based methods [20]-[24].

In the early stage of the development of sensorless control, a recursive least-squares algorithm was used to estimate the rotor position and speed, which was only applicable to sensorless control at extremely low speed [10]. To further increase the accuracy of rotor position estimation, neural network [11], [12] and fuzzy logic [13] control methods were designed. Through the comparison, it was found that the effect of rotor position estimation is accurate, but the design of control parameters is complicated [14]. A sensorless voltage control scheme is proposed, which can achieve high-resolution rotor position estimation [15].

Recently, methods based on flux-linkage and inductance characteristics have been studied. A high-frequency pulse was injected into the non-excitation phase to obtain the inductance of SRMs [16], [17]. Sensorless control works well only in the initial rotor position estimation and starting process. In [14], the phase voltage and current obtained in real-time were employed to calculate the flux linkage by using an artificial neural network (ANN) inference system. To solve the problem of large memory consumption and complicated calculation, an improved flux linkage comparison method was implemented in [18]. Experimental results showed that the position estimation accuracy is acceptable. In [19], a position sensorless torque control method was proposed to reduce torque ripple.

The phase inductance slope zero-crossing detection method has been continuously discussed and developed. The zero-crossing point was used as the commutation point to drive SRMs [20]. For an SRM with 12/8 pole structure, the excitation region of each phase was fixed in [7.5°, 22.5°]. Obviously, the lagged turn-ON angle is very detrimental to the initial current

Manuscript received May 8, 2021; revised Sept 24, 2021; accepted Oct 9, 2021. This work was supported by the National Natural Science Foundation of China under Project 51875261, and the Natural Science Foundation of Jiangsu Province of China under Project BK20180046. (*Corresponding author: Xiang Tian and Gang Lei*)

X. Sun, X. Tang, X Tian, are with the Automotive Engineering Research Institute, Jiangsu University, Zhenjiang 212013, China (email: xdsun@ujs.edu.cn, tangxigntaoh@163.com, auzn0009@163.com).

G. Lei and Y. Guo are with the School of Electrical and Data Engineering, University of Technology Sydney, Sydney, NSW 2007, Australia (e-mail: Gang.Lei@uts.edu.au, Youguang.guo-1@uts.edu.au).

J. Zhu is with the School of Electrical and Information Engineering, University of Sydney, NSW, 2006, Australia (e-mail: jianguo.zhu@sydney.edu.au).

rise, and the lagged turn-OFF angle would cause excessive negative torque [21]. The position estimation method based on the zero-crossing of the phase inductance slope is similar to the phase current gradient method [22]. The characteristic rotor position of this method is to detect the aligned position of the rotor pole and stator pole. However, the detected feature points may be inaccurate due to interference pulse signals generated at the moment of turn-ON and near the feature points. To improve the accuracy of rotor feature position detection, a joint position feature point detection method was proposed [23]. The intersection of the transformer electromotive force and motional electromotive force was used as a feature detection point. It was pointed out that the joint sensorless detection method is only used in the case of medium speed [24]. Therefore, a new slope zero-crossing detection method was proposed to expand the applicable speed range, but there is no solution to the interference signal.

The position sensorless control and fault-tolerant control (FTC) are closely related to each other. In extreme cases, when all position signals are lost, the only way to maintain fault-tolerant operation is to use sensorless control methods. The early fault-tolerant control for SRM was mainly for diagnosis and fault-tolerant control of inverter faults. In [25], a method to detect inverter faults using a neural genetic model is applied. The fault diagnosis is effective, but the fault-tolerant control is not effective. subsequently, an inverter with fault-tolerant function was proposed [26], [27]. This inverter can perform real-time diagnosis and fault-tolerant control. The genetic algorithm (GA) based method [28] were proposed. These methods are effective in detecting faults. A fault diagnosis method of position signal based on edge prediction was proposed [29]. And a fault-tolerant control strategy combining hardware and software was proposed to address the failure of the power inverter. Two sensorless methods and a position sensor were used for the maximum-likelihood voting algorithm to achieve FTC. This method can reduce the number of position sensors. In [30], a sensorless fault-tolerant algorithm was proposed. It can capture at least a single-phase alignment position for both normal and FTC operations.

B. Contributions

In this paper, an error band is established by the phase interval of feature points between the phases, which improves the accuracy of capturing feature points. When a position signal is lost, the FTC is used to improve system stability. The proposed sensorless algorithm with FTC overcomes problems, such as additional hardware, look-up table and a large number of calculations. The main contributions of this paper are listed as follows.

1) In the proposed model, the rising start and maximum inflection points of phase inductance are detected using the electrical terminals. Consequently, it does not require additional hardware. Via establishing the reference time of the characteristic inflection point for diagnosis and fault tolerance of the position signal, this method can effectively eliminate the interference signal.
2) A fault-tolerant algorithm is proposed by fully considering the unbalance inductance case. The proposed fault-tolerant control is not only applicable to four-phase motors but also can be extended to motors with different phases.
3) Experiments and simulations show that the positionless control with FTC is suitable for a wide speed range. Therefore, the speed regulation performance of the SRM system is greatly improved.

C. Paper organization

The rest of this paper is organized as follows. In Section II, the motor model is described, and the method of non-sensor control for a segmented-rotor SRM (SSRM) is proposed. In Section III, principles and implementations of the proposed position sensorless control with FTC under both low-speed and high-speed operations are introduced. Simulations for further analysis are established in Section IV. The experimental results of the proposed strategy are given in Sections V, followed by the conclusion.

II. Switched Reluctance Motor Drive

A. Structure of the four-phase 16/10 SRM

Fig. 1 (a) shows the topology of a segmented-rotor switched reluctance motor (SSRM) and the inductance change with the segmented rotor position. The magnetic flux of the SSRM consists of the excitation teeth, passes through the segmented rotor, and then returns to the excitation teeth from the adjacent auxiliary poles to form an excitation circuit. Therefore, compared with conventional SRM, the magnetic circuit of SSRM is shorter, which makes SSRM have a lower loss and higher efficiency. This SSRM is mainly composed of the winding, isolator, 8 excited poles, 8 auxiliary poles, and segmented rotor that the 10 segmented rotors are embedded in non-magnetic isolators (aluminum). During a complete inductance cycle shown in Fig. 1 (b), the inductance changes slightly before the rotor rotate to θ_1. As the rotor rotates from θ_1 to θ_2, the inductance increases due to the decrease of the reluctance. When the rotor rotates from θ_2 to θ_3, the inductance decreases as the reluctance increases.

The phase voltage equation of the SRM is given as

$$\psi_{ph} = Li = N^2 i / R_{\mathrm{m}} \tag{1}$$

$$U(t) = Ri(t) + [d\psi(\theta, i)]/dt \tag{2}$$

where U, R, i, and ψ denote the phase voltage, phase resistance, phase current, and phase flux linkage, respectively, θ stands for the rotor angular position, N represents the number of winding turns, and R_m stands for the total magnetic reluctance.

B. System description

Fig. 2 shows the overall drive system of the four-phase 16/10 SRM. This drive system consists of a switching converter part for applying a switching pulse to the phase winding, a signal conditioning part for regulating the phase voltage and phase current signals, and a control part for controlling the operating conditions. The switching converter has two switches and two diodes per phase, and each phase uses an independent asymmetrical bridge converter.

The rotor position is estimated by the phase current and phase voltage, and it is accurately judged by the corresponding algorithm. Meanwhile, the FTC of the position signal is performed. After the accurate rotor position signal and speed signal are obtained, the torque control and speed control will be performed. Finally, the turn-ON and turn-OFF signals will be outputted to the power inverter.

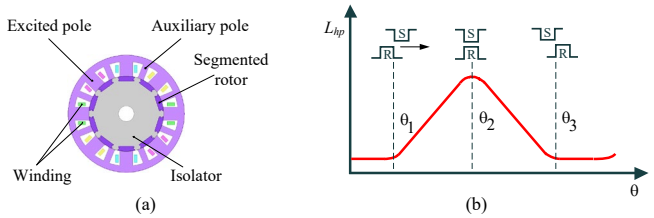

Fig. 1. Structure of the four-phase 16/10 SSRM and the inductance profile.

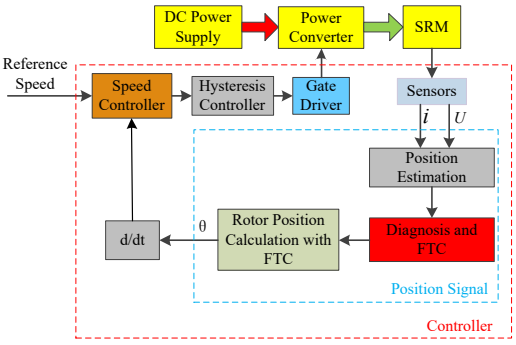

Fig. 2. SRM drive structure of position sensorless control with FTC.

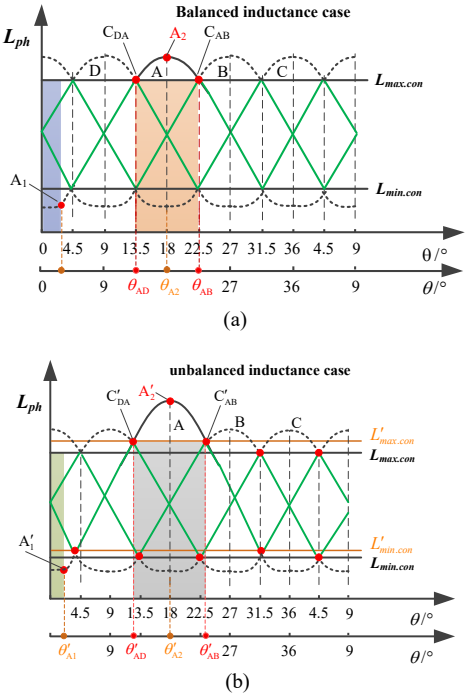

Fig. 3. Diagram of the four-phase inductance under balanced and unbalanced conditions.

III. Principle of the Proposed Position Sensorless Method with FTC

A. Characteristics of the inductance point

Traditionally, the phase inductance cannot be fully calculated and obtained even if it exists throughout the operating cycle. The phase current is discontinuous in current chopper control (CCC) mode and angular position control (APC) mode. When the phase current decays to zero, the value of the phase inductance cannot be calculated. Therefore, a full-cycle inductance can only be obtained by injecting a detection signal into the unexcited phase. However, complete phase inductance is not always required in practical applications. The phase inductance can be set to zero without any calculations when the phase current is zero. Therefore, the phase inductance can be expressed as

$$L=\begin{cases}\left[\int (U-Ri)dt\right]/i, & i>0\\ 0, & i=0\end{cases} \tag{3}$$

Therefore, the selection of inductance characteristic points is crucial to estimate the rotor position. As shown in Fig. 3 (a), a rotor position estimation scheme is proposed based on the rising start point A_1 and the maximum inductance inflection point A_2 [30]. Another scheme was proposed based on the intersection point of the phase inductances [31]. In the balance inductance case, the rotor position estimation is accurate. However, the physical parameters of each phase are limited by the manufacturing accuracy, materials, and environment. And there is no guarantee that the parameters of each phase are exactly the same. There are slight differences in inductance of different phases can be considered as the same inductance. But in actual use, not every motor will be tested whether the inductance of each phase is balanced. As depicted in Fig. 3 (b), the positions of the rising start point A'_1, the maximum inductance inflection point A'_2 and the intersection of the adjacent phase inductances (C'_{DA} and C'_{AB}) have changed under unbalanced inductance conditions, which leads to the increased error of rotor position.

Since the sampling period is short enough, the phase inductance slope can be obtained by

$$\frac{dL}{dt}=\frac{\Delta L}{\Delta T}=\frac{L(\mathrm{k}+1)-L(\mathrm{k})}{T_s} \tag{4}$$

where L, U, R, i, and t are the calculated phase inductance, applied voltage, phase resistance, phase current, and the time, respectively. $L(k)$ and $L(k+1)$ are the inductance at the (k)th and $(k+1)$th sampling instants, and T_s is the sampling time.

Under CCC, The phase current is limited to a range by chopping. The voltage balance equations in the rising and falling areas can be expressed by

$$\begin{aligned}U_{\mathrm{dc}}&=2U_{dio}+Ri_{+}+\frac{d\psi}{di_{+}}\frac{di_{+}}{dt}+\frac{d\psi}{d\theta}\frac{d\theta}{dt}\\&=2U_{dio}+Ri_{+}+L(\theta,i)\frac{di_{+}}{dt}+i\frac{dL_{ph}}{d\theta}\omega\end{aligned} \tag{5}$$

$$0 = 2U_{dio} + Ri_{-} + \frac{d\psi}{di_{-}}\frac{di_{-}}{dt} + \frac{d\psi}{d\theta}\frac{d\theta}{dt}$$

$$= 2U_{dio} + Ri_{-} + L(\theta,i)\frac{di_{-}}{dt} + i\frac{dL_{ph}}{d\theta}\omega \tag{6}$$

where U_{dc} is the phase winding voltage, R the phase resistance, i_{+} the current of chopping rising area, i_{-} the current of chopping falling area, ψ the phase flux linkage, and U_{dio} the voltage drop across the diode and transistor.

Around the detection position, i_{+} is close to i_{-} if the chopper width Δi is small enough. Then, the inductance with rotor position and current can be obtained from (5) and (6).

$$U_{dc} = L(\theta,i)\left(\frac{di_{+}}{dt} - \frac{di_{-}}{dt}\right) \tag{7}$$

where di_{+}/dt and di_{-}/dt can be easily obtained by dividing chopper width by rising time and falling time.

$$L(\theta,i_{ph}) = U\Big/\left(\frac{di_{+}}{dt} - \frac{di_{-}}{dt}\right) \tag{8}$$

The inductance value can be calculated at low speed.

B. Phase inductance slope zero-crossing detection

CCC is employed during the low-speed operation. According to (8), the phase inductance value can be calculated. The rising start point point A_1 of the inductance can be accurately captured. The turn ON/OFF angles of the SRM are constant under CCC control. Therefore, the calculation of the rising start point A_1 is expressed as

$$\begin{cases} \dfrac{dL_{A_1-}}{d\theta} = \dfrac{dL}{d\theta}\Big|_{\theta<\theta_{A_1}} = 0 \\ \dfrac{dL_{A_1+}}{d\theta} = \dfrac{dL}{d\theta}\Big|_{\theta>\theta_{A_1}} > 0 \end{cases} \tag{9}$$

The maximum inductance inflection point A_2 can be expressed as

$$\begin{cases} \dfrac{dL_{A_2-}}{d\theta} = \dfrac{dL}{d\theta}\Big|_{\theta<\theta_{A_2}} > 0 \\ \dfrac{dL_{A_2+}}{d\theta} = \dfrac{dL}{d\theta}\Big|_{\theta>\theta_{A_2}} < 0 \end{cases} \tag{10}$$

The phase voltage equation of SRM is expressed as

$$U_{ph} = Ri_{ph} + \frac{d(L\cdot i_{ph})}{dt} = Ri_{ph} + L\frac{i_{ph}}{dt} + i_{ph}\omega\frac{dL}{d\theta} \tag{11}$$

Equation (11) can be summarized as the current change rate with respect to time, as shown in (12). Here, ω represents the rotor speed.

$$\frac{di_{ph}}{dt} = \frac{U_{ph} - Ri_{ph} - i_{ph}\omega\dfrac{dL}{d\theta}}{L} \tag{12}$$

Since the value of Ri_{ph} is much smaller than U_{ph}, it can be ignored and (12) can be rewritten as (13). As can be seen from the equation, when the inductance change rate decreases, the phase current increases.

$$\frac{di_{ph}}{dt} \approx \frac{U_{ph} - i_{ph}\omega(dL/d\theta)}{L} \tag{13}$$

The corresponding position pulse signals are obtained by acquiring the characteristic points A_1 and A_2, The speed of the rotor can be calculated by (14).

$$\omega = \frac{\Delta\theta}{\Delta t} \tag{14}$$

At high speeds, APC is applied. The term Ri_{ph} (known as the resistance voltage drop) in (11) is ignored. The phase voltage U_{ph} is represented as

$$U_{ph} \approx \omega L\frac{di_{ph}}{d\theta} + \omega i_{ph}\cdot\frac{dL_{hp}}{d\theta} \tag{15}$$

Assuming that the rotor pole begins to overlap with the excited pole at the rotor position θ_{ov}, (15) is rewritten as follows according to the rotor position, i.e., when the rotor pole approaches θ_{ov} or when the rotor pole has already passed θ_{ov}:

$$U_{ov-} = \omega L_{ov-}\frac{di_{ov-}}{d\theta} + \omega i_{ov-}\cdot\frac{dL_{ov-}}{d\theta} \tag{16}$$

$$U_{ov+} = \omega L_{ov+}\frac{di_{ov+}}{d\theta} + \omega i_{ov+}\cdot\frac{dL_{ov+}}{d\theta} \tag{17}$$

Here, (16) represents the voltage balance equation when the rotor position approaches θ_{ov} and (17) denotes that when exceeding. If it is assumed that the inductance does not change in (16), but does change in (17) rapidly to θ, (16) and (17) can be rewritten as

$$\frac{di_{ov-}}{d\theta} = \frac{U_{ov-}}{\omega L_{ov-}} \tag{18}$$

$$\frac{di_{ov+}}{d\theta} = \frac{\left(U_{ov+} - \omega i_{ov+}\cdot dL_{ov+}/d\theta\right)}{\omega L} \tag{19}$$

Considering that the voltage is smaller than the back EMF during the overlap period, the results of (18) and (19) can be expressed as (20). Note that the boundary condition of the current slope change is given at the overlap angle θ_{ov}:

$$\begin{cases} \dfrac{di_{ov-}}{d\theta} = \dfrac{di_{ph}}{d\theta}\Big|_{\theta<\theta_{ov}} > 0 \\ \dfrac{di_{ov+}}{d\theta} = \dfrac{di_{ph}}{d\theta}\Big|_{\theta>\theta_{ov}} < 0 \end{cases} \tag{20}$$

Under balanced inductance case, the calculation of inductance is accurate. The calculation of selected feature points can be accurately obtained. However, during the experiment, it was found that the error of the rotor position estimation was still relatively large. This is caused by unbalanced phase inductance and zero-crossing interference signals.

C. Principle of interference signals elimination

The detection of the maximum inductance inflection point is accurate in Fig. 4. However, the detection of the rising start point is unstable because of many interfered factors. Hence, after implementing basic sensorless control, this paper proposes a method to improve the detection accuracy and fault tolerance.

The proposed model is divided into four parts, as shown in Fig. 5. The first part is the calculation of inductance, which is the basis of extracting the characteristic value of inductance. The calculated inductance is compared with the characteristic inflection point to obtain a special position signal. The second part is to calculate the rising start point and the maximum inductance inflection point using the slope zero-crossing detection, and the error correction algorithm to eliminate the interference signal. The next step is to calculate the corrected rotor position and speed using FTC, as shown in Fig. 5. The rotor position information is calculated by extracting the characteristic position. The final step is to acquire the commutator point of the motor and provide the commutation information to the converter.

As shown in Fig. 6, In order to eliminate the interference signal near point C_1, the maximum inductance inflection point A_2 is used as a reference point. Establish the reference time of the point C_1 through the reference point, and set the allowable error band. In this way, the accurate zero-crossing position of point C_1 is determined. The efficiency of eliminating interference signals is subject to the design of the error band. The wider the error band is to reduce the acquisition of inductance characteristic points. The narrower the error band is beneficial to the elimination of interference signals, because some interference signals outside the error band will not be mistaken for characteristic points.The process of selecting the range of the error band: First, estimate the time t_{c1_ref} when the next feature point appears through the current speed. After that, the error band is selected. The elimination of interference signals gradually weakens as the error band increases. The error band is too small so that the feature point detection may be lost due to the delay in hardware calculation. The error band selected in this paper is 5% (the time required for the rotor angle of 1.8° is at different speeds).

Fig. 7 shows the detection algorithm of the feature inductance inflection points of the excitation phase eliminating interference signals at low speed. The rotor position signal and speed information are obtained through the signal extraction of the characteristic points, and the speed is calculated by (14).

In summary, for both low-speed and high-speed sensorless control, it is feasible to use the detection of the rising start point and the inflection point of the maximum inductance of the excitation phase. However, there are still many aspects that can be improved. For example, the detection accuracy of the rising start point needs to be further improved, and the FTC under signal detection failure needs further exploration.

D. Fault resilient strategies for position sensorless method

The acquisition and accuracy of the position signal are critical in an SRM system with sensorless control. Compared with the loss of multi-phase rotor signal, the loss of one-phase rotor signal is most encountered in the experiment.In this section, an FTC method is discussed to overcome the problem of signal loss in sensorless control.

As shown in Figs. 7 and 10, the rising start detection of phase inductance is easily affected by the interference signal, leading to failure of accurate position signal acquisition. Using adjacent phases to establish the corresponding reference time and allowable error band can effectively screen and acquire the characteristic point signals. In addition, when the signal detection fails, the redundant detection points and FTC are used to complete the reconstruction of the position signal.

According to the relevant structural design theory of the SRM [15], it can be seen that the phase inductance is not center symmetrical, as shown in Fig. 8. The angle relationship is established by the phase interval among the inflection points of

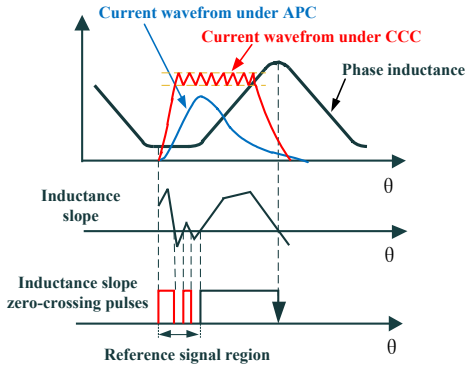

Fig. 4. Phase inductance slope zero-crossing detection.

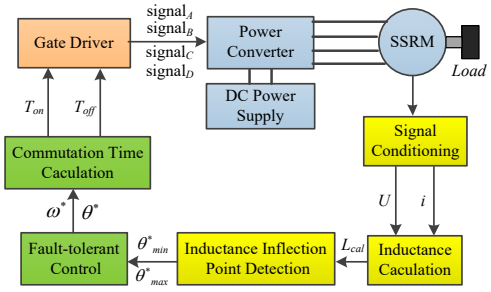

Fig. 5. Principle diagram of the phase inductance slope detection.

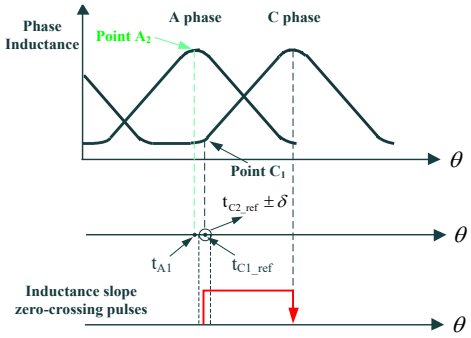

Fig. 6. Detection signal diagram under APC control.

the phase inductance. $\Delta\theta_{12}$ represents the phase interval between inductance point A_2 and inductance point C_1. $\Delta\theta_{23}$ represents the phase interval between inductance point C1 and inductance point C_2. $\Delta\theta_{34}$ represents the phase interval between inductance point C_2 and inductance point A_1. The $\Delta\theta_{12}$ $\Delta\theta_{23}$, and $\Delta\theta_{34}$ can be calculated from the structural parameters of the motor. And they are utilized as compensation angle.

The detected points C_1 and C_2 generate two pulse signals as position signals, which are used to calculate the rotor position and rotor speed under normal operation. The turn ON/OFF angles of the next phase are obtained based on the position and speed signals. The normal collection of the detected points C_1

and C_2 can ensure the rapid update of the rotor position information and improve the accuracy of the control.

The feature point signal failure detection process is shown in Fig. 9. t represents the real-time of the rotor running in a rotor cycle. It has been waiting for feature point detection before entering the error band. In [t_{C1_ref}-δ, t_{C1_ref}+δ], the feature point is checked for existence. After exceeding the detection range of the error band, if the characteristic point does not appear, it is determined that the rotor position is lost. Use the redundant feature points of other phases to supplement.

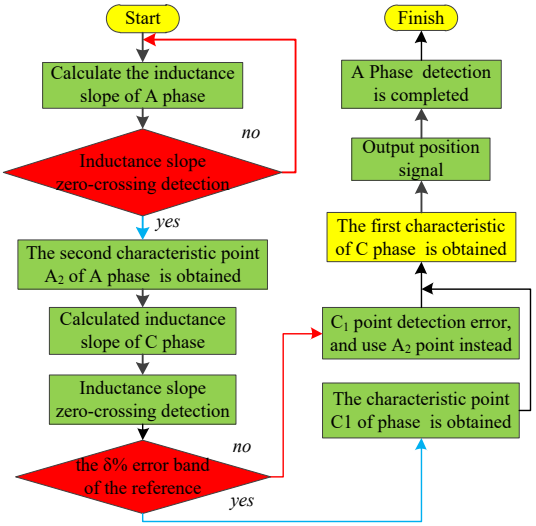

Fig. 7 Algorithm for inductance peak detection.

In the vicinity of the zero-crossing detection position of the maximum inductance, the number of interference signals is very small, so its position detection is accurate. Under abnormal operation, when the signal of point C_1 cannot be obtained normally, point A_2 has higher accuracy than other feature points and is adjacent to C_1. Point C_1 is replaced by point A_2, and the calculation of the rotor speed needs to supplement the corresponding angular interval $\Delta\theta_{12}$ and time interval Δt_{12}. The basic algorithm flow chart is shown in Fig. 10 (a).

When the signal of the characteristic point C_2 of the C phase cannot be obtained normally, point C_2 is replaced by point A_1. After the signal at point A_1 is filtered by the error band, the accuracy of the signal can be guaranteed. The rotor speed calculation supplements the corresponding angular interval $\Delta\theta_{34}$ and time interval Δt_{34}. The basic algorithm flow chart is shown in Fig. 10 (b).

When the signals of the characteristic points C_1 and C_2 are missing, the fault tolerance control is completed by replacing the C_1 and C_2 with the points A_2 and A_1. The rotor speed and position information needs to be supplemented with time intervals and angular intervals. However, the reduction of rotor position signal sampling will reduce the accuracy of the control.

$$\omega_{c1} = (\Delta\theta_{23} + \Delta\theta_{12})/\Delta t_{13} \quad (21)$$

$$\omega_{c2} = (\Delta\theta_{23} + \Delta\theta_{34})/\Delta t_{24} \quad (22)$$

$$\omega_{c12} = (\Delta\theta_{12} + \Delta\theta_{23} + \Delta\theta_{34})/\Delta t_{14} \quad (23)$$

where $\Delta\theta_{ij}$ represents the angle interval between point i and point j, and Δt_{ij} represents the time interval between point i and point j.

When the signal acquisition of the characteristic point C_1 is faulty, point A_2 replaces the characteristic point C_1. The compensated angle $\Delta\theta_{ij}$ is $\Delta\theta_{12}$. The rotor speed is calculated by (21). When the signal acquisition of the feature point C_2 is faulty, point A_1 replaces the feature point C_2. The compensated angle is $\Delta\theta_{34}$. The formula (22) is used to calculate the rotor speed. When the signals of characteristic points C_1 and C_2 are abnormal, points A_2 and A_1 are used to replace points C_1 and C_2, respectively. The compensated angle is $\Delta\theta_{12}+\Delta\theta_{34}$. The rotor speed is calculated by (23).

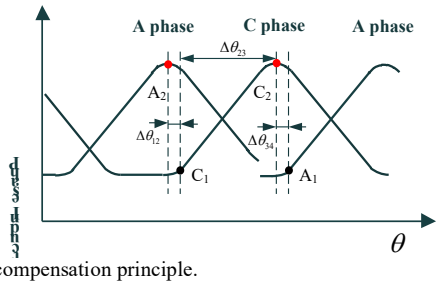

Fig. 8. Angle compensation principle.

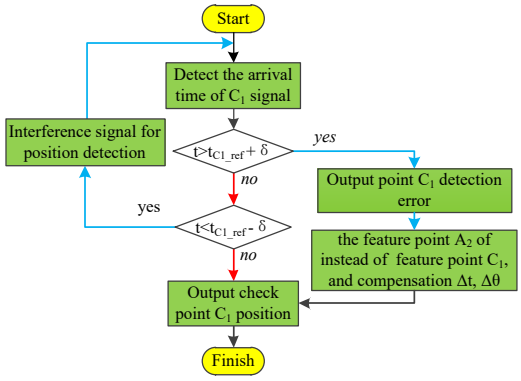

Fig. 9. Feature point signal failure detection diagnosis algorithm.

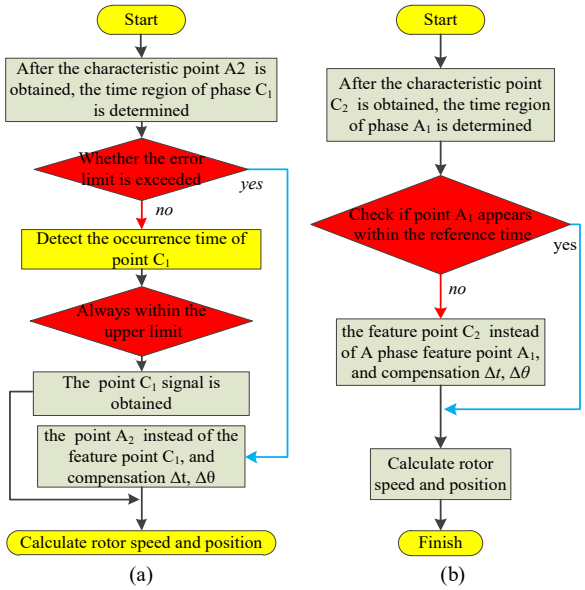

Fig. 10. Fault-tolerant algorithm for feature point detection.

IV. Simulation Results

In this section, the proposed sensorless algorithm with the FTC system is verified by SIMULINK in MATLAB. The simulation environment is selected the same as the experiment environment. Therefore, the modeled 16/10 SRM and asymmetric half-bridge converter are included. Also, the proposed algorithm is operated step by step. Two pulse signals are generated at the rising start point and the maximum point of the inductance. The rotor speed, the rotor position and the turn ON/OFF time of the next phase are calculated from the pulse signal. When the signal is disturbed, the position signal can still be accurately captured.

Fig. 11 (a) shows the calculation of the inductance at 600 r/min. One signal is to detect the rising start point of the inductance and calculate the excitation point of the next phase. The other signal is to detect the maximum point of the inductance and establish a reference time for the rising start point of the next phase inductance. Similarly, Fig. 11 (b) demonstrates the calculation of the inductance at 3200 r/min.

In Figs. 12 (a) and (c), at the speed of 600 r/min and when a step load is applied at 0.24 s, the rotor speed can return the required speed quickly and smoothly. However, in the absence of FTC algorithms, when the rotor position signal is lost at 0.43 s, the rotor speed fluctuates, and it is difficult to stabilize. The stability of the system deteriorates with the increase of excitation phase current. As illustrated in Figs. 12 (b) and (d), the stability of the system drops dramatically for applications that require higher speeds.

In Figs 13 (d) and 14 (d), an FTC signal is generated when the estimated rotor position signal is lost at different speeds. The phase current and drive signals are operating normally due to fault-tolerant control as shown in Fig. 13 and Fig. 14. In Fig. 15, the operation of the motor is more stable under the FTC algorithm. The stability of the SRM system can be improved greatly as well. Then, the effectiveness of the proposed control method under unbalanced inductance is verified. Reducing the flux linkage data of phase A, Fig. 16 shows the calculated contour of the inductance and the rotor position estimation error. The result proves that the algorithm is also effective for unbalanced inductance. There is no significant difference in the position estimation error obtained under balanced inductance and unbalanced inductance.

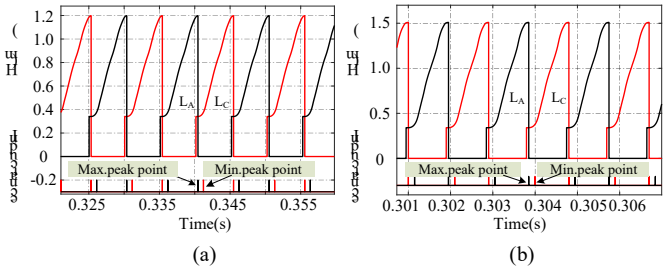

Fig. 11. Simulation results of inductance calculation: (a) at low speed (600 r/min), and (b) at high speed (3200 r/min).

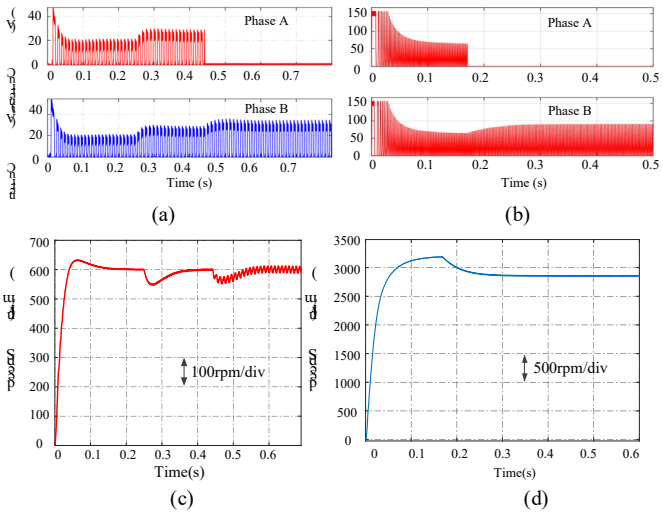

Fig. 12. Simulation results without fault tolerance control: (a) phase current at low speed, (b) phase current at high speed, (c) rotor speed estimation at low speed, and (d) rotor speed estimation at high speed.

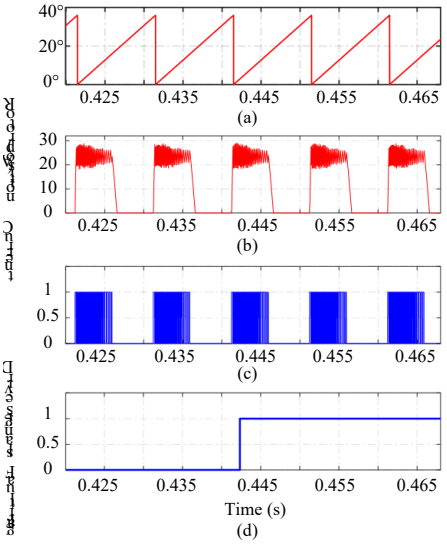

Fig. 13. Simulation results with fault-tolerance control at low speed: (a) rotor speed estimation, (b) phase current, (c) dirive signals, and (d) fault flag.

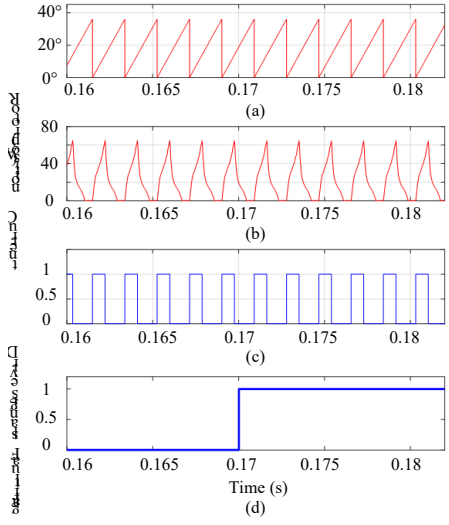

Fig. 14. Simulation results with fault-tolerance control at high speed: (a) rotor speed estimation, (b) phase current, (c) dirive signals, and (d) fault flag.

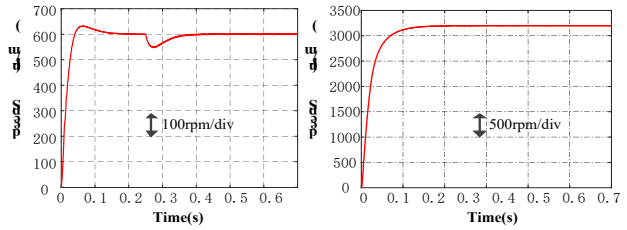

(a) (b)

Fig. 15. Rotor speed estimation with FTC: (a) at low-speed, and (b) at high-speed.

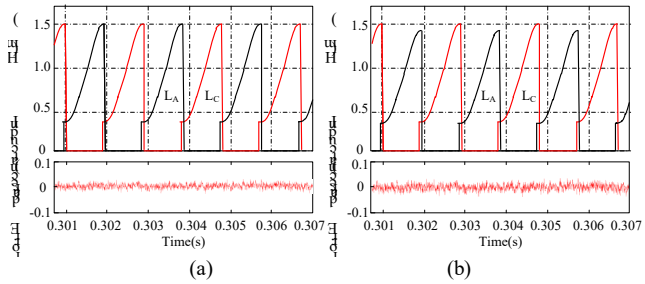

(a) (b)

Fig. 16. Simulation results on inductance calculation and position estimation error: (a) Balanced inductance, and (b) Unbalanced inductance.

V. Experimental Results

To validate the proposed method, experiments have been performed on a 16/10 structure SSRM. Table I lists its main specifications. Fig. 17 shows the experimental testbed. As shown, the experimental testbed mainly consists of a dSPACE controller, an asymmetric half-bridge power converter and a magnetic powder brake.

Fig. 18 shows the calculated inductance of phase A, the detected rising start peak point of phase inductance, the calculated excitation point of the next phase, and the redundant backup signal.

The estimated rotor position and the measured rotor position are shown in Figs. 18 (a) and (b). The position of the rotor is accurately calculated at 600r/min and 3200r/min. The average error of rotor position estimation is 7.3% when phase A and phase C are used. When all phases are utilized to estimate the rotor position without considering the hardware burden, the average error is reduced by 3.2%. The estimated ranking position and the measured rotor position are shown in Fig. 19. The proposed sensorless method without FTC can achieve the reference speed under a step load (0 to 1Nm) at 0.15s, and then the motor cannot achieve the reference speed under a step load (1 to 2Nm) at 0.27s, as shown in Fig. 20. However, The PWM (Pulse Width Modulation) of the fault phase A cannot be calculated and output because the rotor position is lost. The stability of the SRM system is significantly reduced, including increased torque ripple shown in Figs. 20 (a) and (b), unstable rotor speed shown in Figs. 20 (c) and (d), and abnormally increased phase current shown in Figs. 20 (e) and (f).

Compared with Fig. 20, Fig. 21 shows the experimental results of position sensorless control with fault tolerance. A faul of phase A is designed at 600/min and 3200r/min. As shown in Figs. 21 (a) and (b), once the estimated rotor signal is lost, the corresponding FTC is enforced. The estimated speed can effectively track the speed reference in both low-speed and high-speed modes, because the lost rotor signal is reconstructed by the redundant position signal in Figs. 21 (c) and (d). As shown in Fig. 22, the estimated rotational speed can track the speed references well in acceleration and deceleration modes. The classic pulse injection-based sensorless starting method is utilized to obtain the initial motor rotor position signal [16].

TABLE I
SPECIFICATIONS OF THE SSRM

Parameters	Unit	Value
Rated power	kW	1.8
Rated torque	Nm	2
Rated voltage	V	60
Efficiency	%	85
Axial length	mm	80
Outer diameter	mm	128

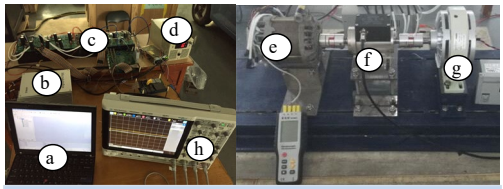

(a).PC, (b).dSPACE, (c).Power converter and drive circuit, (d).Power supply, (e).16/10 SSRM, (f).Torque and speed sensor, (g).Magnetic powder brake, (h).Oscilloscope

Fig. 17. Photograph of the experimental testbed.

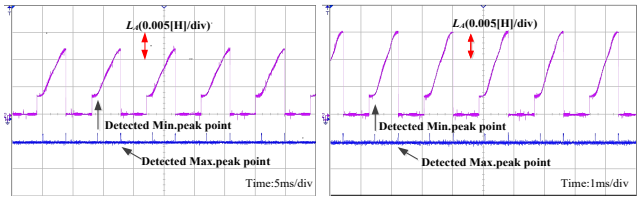

(a) (b)

Fig. 18. Experimental results of inductance calculation: (a) at low speed (600 r/min), and (b) at high speed (3200 r/min).

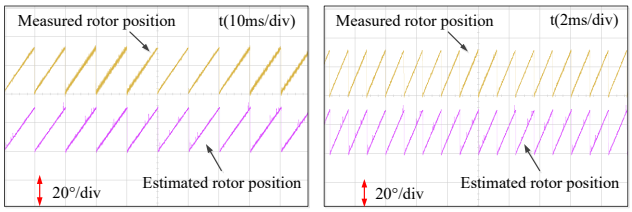

(a) (b)

Fig. 19. Experimental results of Rotor speed estimation: (a) in low-speed (600 r/min), and (b) in high- speed (3200 r/min).

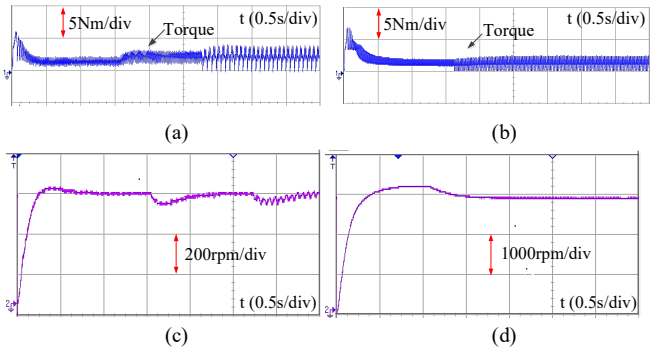

(a) (b)

(c) (d)

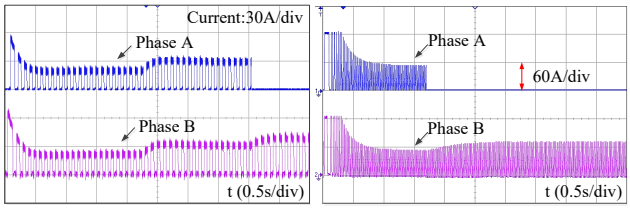

Fig. 20. Experimental results without FTC: (a) torque and phase current at low speed, (b) torque and phase current at high speed, (c) speed curve (600 r/min), (d) speed curve (3200 r/min), (e) phase current curve at low speed, and (f) phase current curve at high speed.

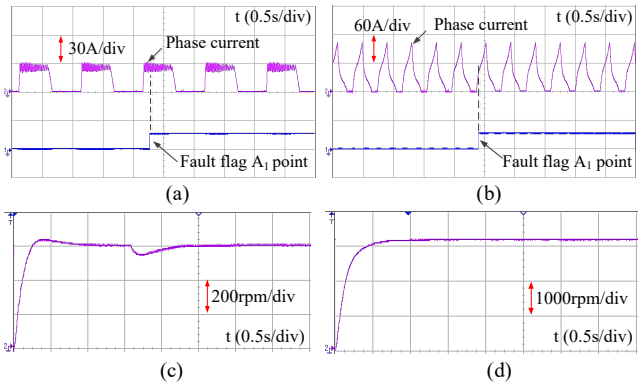

Fig. 21. Experimental results with FTC: (a) phase current and fault-tolerant signals at low speed, (b) phase current and fault-tolerant signals at high speed, (c) speed curve (600 r/min), and (d) speed curve (3200 r/min).

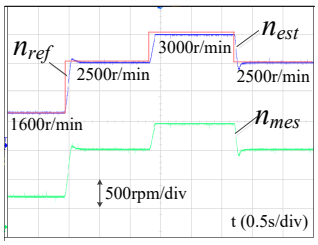

Fig. 22. Rotor speed estimation result under the speed transient mode.

VI. Conclusion

This paper proposed a reference time-based diagnosis and a position sensorless control with fault-tolerant ability for SRMs. The time error band is established according to the reference time, and the rotor position is captured in an electrical cycle through the inductance slope signal. Consequently, the stability of the system can be greatly improved by eliminating a large number of error signals and capturing accurate position signals. Meanwhile, this method owns fault tolerance. The estimation of the feature position in each phase is completely independent. When some position signals are lost, this algorithm can make full use of the relationship among phase inductances to establish a new position pulse. Furthermore, the proposed sensorless control of the motor can be performed at both high and low speeds. The experimental results have verified the effectiveness of the proposed control strategy.

References

[1] X. Sun, K. Diao, G. Lei, Y. Guo, and J. Zhu, "Direct torque control based on a fast modeling method for a segmented-rotor switched reluctance motor in HEV application," *IEEE J. Emerg. Sel. Topics Power Electron.*, vol. 9, no. 1, pp. 232-241, Feb. 2021.

[2] H. Ro, D. Kim, H. Jeong, and K. Lee, "Tolerant control for power transistor faults in switched reluctance motor drives," *IEEE Trans. Ind. Appl.*, vol. 51, no. 4, pp. 3187-3197, July-Aug. 2015.

[3] K. Diao, X. Sun, G. Lei, Y. Guo, and J. Zhu, "Multimode optimization of switched reluctance machines in hybrid electric vehicles," *IEEE Trans. Energy Convers.*, vol. 36, no. 3, pp. 2217-2226, Sep. 2021.

[4] S. Song, G. Fang, R. Hei, J. Jiang, R. Ma, and W. Liu, "Torque ripple and efficiency online optimization of switched reluctance machine based on torque per Ampere characteristics," *IEEE Trans. on Power Electron.*, vol. 35, no. 9, pp. 9608-9616, Sep. 2020.

[5] X. Sun, J. Wu, G. Lei, Y. Guo, and J. Zhu, "Torque ripple reduction of SRM drive using improved direct torque control with sliding mode controller and observer," *IEEE Trans. Ind. Electron.*, vol. 68, no. 10, pp. 9334-9345, Oct. 2021.

[6] X. Guo, R. Zhong, M. Zhang, D. Ding, and W. Sun, "Resonance reduction by optimal switch angle selection in switched reluctance motor," *IEEE Trans. Ind. Electron.*, vol. 67, no. 3, pp. 1867-1877, 2020.

[7] K. Diao, X. Sun, G. Lei, Y. Guo, and J. Zhu, "Multiobjective system level optimization method for switched reluctance motor drive systems using finite element model," *IEEE Trans. Ind. Electron.*, vol. 67, no. 12, pp. 10055-10064, Dec. 2020.

[8] K. Diao, X. Sun, G. Lei, G. Bramerdorfer, Y. Guo, and J. Zhu, "System-level robust design optimization of a switched reluctance motor drive system considering multiple driving cycles," *IEEE Trans. Energy Convers.*, vol. 36, no. 1, pp. 348-357, Mar. 2021.

[9] X. Sun, L. Feng, K. Diao, and Z. Yang, "An improved direct instantaneous torque control based on adaptive terminal sliding mode for a segmented-rotor SRM," *IEEE Trans. Ind. Electron.*, vol. 68, no. 11, pp. 10569-10579, Nov. 2021.

[10] A. Khalil, I. Husain, S. A. Hossain, S. Gopalakrishnan, A. M. Omekanda, B. Lequesne, and H. Klode, "A hybrid sensorless SRM drive with eight and six-switch converter topologies," *IEEE Trans. Ind. Appl.*, vol. 41, no. 6, pp. 1647–1655, Nov./Dec. 2005.

[11] Y. Cai, Y. Wang, H. Xu, S. Sun, C. Wang, and L. Sun, "Research on rotor position model for switched reluctance motor using neural network," *IEEE/ASME Trans. Mechatron.*, vol. 23, no. 6, pp. 2762-2773, 2018.

[12] C. A. Hudson, N. S. Lobo, and R. Krishnan, "Sensorless control of single switch-based switched reluctance motor drive using neural network," *IEEE Trans. Ind. Electron.*, vol. 55, no. 1, pp. 321–329, Jan. 2008.

[13] L. Xu and C. Wang, "Accurate rotor position detection and sensorless control of SRM for super-high speed operation," *IEEE Trans. Power Electron.*, vol. 17, no. 5, pp. 757–763, Sep. 2002.

[14] S. Paramasivam, S. Vijayan, M. Vasudevan, R. Arumugam, and R. Krishnan, "Real-time verification of AI based rotor position estimation techniques for a 6/4 pole switched reluctance motor drive," *IEEE Trans. Magn.*, vol. 43, no. 7, pp. 3209–3222, Jul. 2007.

[15] F. J. Anayi and M. M. A. A. Ibraheemi, "Estimation of rotor position for permanent magnet synchronous motor at standstill using sensorless voltage control scheme," *IEEE/ASME Trans. Mechatron.*, vol. 25, no. 3, pp. 1612-1621, 2020.

[16] G. Pasquesoone, R. Mikail, and I. Husain, "Position estimation at starting and lower speed in three-phase switched reluctance machines using pulse injection and two thresholds," *IEEE Trans. Ind. Appl.*, vol. 47, no. 4, pp. 1724–1731, Jul./Aug. 2011.

[17] A. Khalil, S. Underwood, I. Husain, H. Klode, B. Lequesne, S. Gopalakrishnan, and A. M. Omekanda, "Four-quadrant pulse injection and sliding-mode-observer-based sensorless operation of a switched reluctance machine over entire speed range including zero speed," *IEEE Trans. Ind. Appl.*, vol. 43, no. 3, pp. 714–723, May/Jun. 2007.

[18] Y. Chang, K. W. E. Cheng, and S. L. Ho, "Type-V exponential regression for online sensorless position estimation of switched reluctance motor," *IEEE/ASME Trans. Mechatron.*, vol. 20, no. 3, pp. 1351-1359, 2015.

[19] C. Gan, Q. Sun, Y. Chen, J. Si, J. Wu, and Y. Hu, "A position sensorless torque control strategy for switched reluctance machines with fewer current sensors," *IEEE/ASME Trans. Mechatron.*, pp. 1-1, 2020.

[20] I. Miki, H. Noda, and R. Moriyama, "A sensorless drive method for switched reluctance motor based on gradient of phase inductance," in *Proc. Int. Conf. Elect. Mach. Syst.* , pp. 615–618, Nov. 2003.

[21] X. Sun, J. Wu, G. Lei, Y. Cai, X. Chen, and Y. Guo, "Torque modeling of a segmented-rotor SRM using maximum-correntropy-criterion-based LSSVR for torque calculation of EVs," *IEEE J. Emerg. Sel. Topics Power Electron.*, vol. 9, no. 3, pp. 2674-2684, Jun. 2021.

[22] J. Cai and Z. Deng, "A position sensorless control of switched reluctance motors based on phase inductance slope," *J. Power Electron.*, vol. 13, no. 2, pp. 264–274, Mar. 2013.
[23] J. Cai and Z. Deng, "A joint feature position detection-based sensorless position estimation scheme for switched reluctance motors," *IEEE Trans. Ind. Electron.*, vol. 64, no. 6, pp. 4352-4360, June 2017.
[24] J. Kim and R. Kim, "Sensorless direct torque control using the inductance inflection point for a switched reluctance motor," *IEEE Trans. Ind. Electron.*, vol. 65, no. 12, pp. 9336-9345, 2018.
[25] L. A. Belfore and A. Arkadan, "A methodology for characterizing fault tolerant switched reluctance motors using neurogenetically derived models," *IEEE Trans. Energy Convers.,* vol. 17, no. 3, pp. 380-384, 2002.
[26] J. F. Marques, J. O. Estima, N. S. Gameiro, and A. J. M. Cardoso, "A new diagnostic technique for real-time diagnosis of power converter faults in switched reluctance motor drives," *IEEE Trans. Ind. Appl.,* vol. 50, no. 3, pp. 1854-1860, 2014.
[27] N. Ali, Q. Gao, C. Xu, P. Makys, and M. Stulrajter, "Fault diagnosis and tolerant control for power converter in SRM drives," *IEEE J. Eng.,* vol. 2018, no. 13, pp. 546-551, 2018.
[28] E. B. Sedrine, J. Ojeda, M. Gabsi, and I. Slama-Belkhodja, "Fault-tolerant control using the GA optimization considering the reluctance torque of a five-phase flux switching machine," *IEEE Trans. Energy Convers.*, vol. 30, no. 3, pp. 927-938, Sept. 2015.
[29] J. Shao, Z. Deng, and Y. Gu, "Fault-tolerant control of position signals for switched reluctance motor drives," *IEEE Trans. Ind. Appl.,* vol. 53, no. 3, pp. 2959-2966, 2017.
[30] J. Cai, Z. Liu, and Y. Zeng, "Aligned position estimation based fault-tolerant sensorless control strategy for SRM drives," *IEEE Trans. on Power Electron.,* vol. 34, no. 8, pp. 7754-7762, 2019.
[31] J. Cai and Z. Deng, "Unbalanced phase inductance adaptable rotor position sensorless scheme for switched reluctance motor," *IEEE Trans. Power Electron.*, vol. 33, no. 5, pp. 4285-4292, 2018.

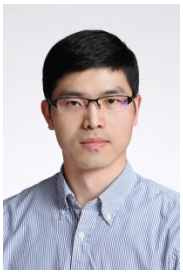

Xiaodong Sun (M'12-SM'18) received the B.Sc. degree in electrical engineering, and the M.Sc. and Ph.D. degrees in control engineering from Jiangsu University, Zhenjiang, China, in 2004, 2008, and 2011, respectively.

Since 2004, he has been with Jiangsu University, where he is currently a Professor in Vehicle Engineering with the Automotive Engineering Research Institute. From 2014 to 2015, he was a Visiting Professor with the School of Electrical, Mechanical, and Mechatronic Systems, University of Technology Sydney, Sydney, Australia. His current teaching and research interests include electrified vehicles, electrical machines, electrical drives, and energy management. He is the author or coauthor of more than 100 refereed technical papers and one book, and he is the holder of 42 patents in his areas of interest. Dr. Sun is an Editor of the IEEE TRANSACTIONS ON ENERGY CONVERSION.

Xingtao Tang was born in Ankang, Shannxi, China, in 1996. He received the B.S. degree in vehicle engineering from Xi'an University of Science and Technology, Xi'an, China, in 2019, and he is currently working toward the M.Sc. degree in Jiangsu University, Zhenjiang, China.

His research interests include position sensorless control and control strategy optimization of switched reluctance motors for electric vehicle propulsion

Xiang Tian was born in Zhenjiang, Jiangsu, China, in 1983. He received the B.S. degree in electrical engineering, M.S. degree in power electronics and power transmission and Ph.D. degree in vehicle engineering from Jiangsu University, Zhenjiang, China, in 2006, 2009 and 2018, respectively. He is currently a lecturer with the automotive engineering research institute, Jiangsu University.

His current research interests include electric vehicles, hybrid electric vehicles, parameter matching, optimal energy control strategy, and vehicle powertrain control.

Gang Lei (M'14) received the B.S. degree in Mathematics from Huanggang Normal University, China, in 2003, the M.S. degree in Mathematics and Ph.D. degree in Electrical Engineering from Huazhong University of Science and Technology, China, in 2006 and 2009, respectively.

He is currently a Senior Lecturer at the School of Electrical and Data Engineering, University of Technology Sydney (UTS), Australia. His research interests include computational electromagnetics, design optimization and control of electrical drive systems and renewable energy systems. He is an Associate Editor of the IEEE TRANSACTIONS ON INDUSTRIAL ELECTRONICS and an Editor of the IEEE TRANSACTIONS ON ENERGY CONVERSION.

Youguang Guo (S'02-M'05-SM'06) received the B.E. degree from Huazhong University of Science and Technology, China in 1985, the M.E. degree from Zhejiang University, China in 1988, and the Ph.D. degree from University of Technology Sydney (UTS), Australia in 2004, all in electrical engineering.

He is currently a Professor at the School of Electrical and Data Engineering, UTS. His research fields include measurement and modeling of properties of magnetic materials, numerical analysis of electromagnetic field, electrical machine design optimization, power electronic drives and control.

Jianguo Zhu (S'93–M'96–SM'03) received the B.E. degree in 1982 from Jiangsu Institute of Technology, Jiangsu, China, the M.E. degree in 1987 from Shanghai University of Technology, Shanghai, China, and the Ph.D. degree in 1995 from the University of Technology Sydney (UTS), Sydney, Australia, all in electrical engineering.

He was appointed a lecturer at UTS in 1994 and promoted to full professor in 2004 and Distinguished Professor of Electrical Engineering in 2017. At UTS, he has held various leadership positions, including the Head of School for School of Electrical, Mechanical and Mechatronic Systems and Director for Centre of Electrical Machines and Power Electronics. In 2018, he joined the University of Sydney, Australia, as a full professor and Head of School for School of Electrical and Information Engineering. His research interests include computational electromagnetics, measurement and modelling of magnetic properties of materials, electrical machines and drives, power electronics, renewable energy systems and smart micro grids.